Available online at www.sciencedirect.com
SCIENCE DIRECT®
International Journal of Heat and Mass Transfer 48 (2005) 4492–4497
International Journal of HEAT and MASS TRANSFER
www.elsevier.com/locate/ijhmt

Partly three-dimensional global modeling of a silicon Czochralski furnace. II. Model application: Analysis of a silicon Czochralski furnace in a transverse magnetic field

Lijun Liu, Koichi Kakimoto *

Research Institute for Applied Mechanics, Kyushu University, 6-1 Kasuga-Koen, Kasuga 816-8580, Japan

Received 8 June 2004; received in revised form 26 January 2005
Available online 19 July 2005

Abstract

A three-dimensional (3D) global analysis was carried out numerically for a small silicon Czochralski (CZ) furnace in a transverse magnetic field by a proposed 3D global model. The modeling was conducted with moderate requirements of computer resources and computation time. Most 3D features of the melt flow and thermal field in the furnace could be reproduced in the modeling. The results showed that the melt–crystal interface shape is three-dimensional and temperature difference over the circumference on the crystal and crucible sidewalls is prominent. The non-uniformity of temperature in the azimuthal direction decreases with increase in distance from the melt region. The influence of a transverse magnetic field on the flow pattern of melt and global thermal field in the furnace was analyzed.

Keywords: Computer simulation; Global modeling; Czochralski method; Transverse magnetic field; Semiconducting silicon

1. Introduction

Application of magnetic fields in silicon CZ growth is an effective method for controlling the melt–crystal interface shape and the melt convection in a crucible, and therefore for improving crystal quality. Active control by applying a transverse magnetic field to silicon CZ growth processes (TMCZ) is gaining more and more attention. The melt flow in a crucible and, hence, the global thermal field within the furnace are principally three-dimensional under the influence of a transverse magnetic field. Although there are many excellent published works on numerical modeling of a TMCZ growth [1–6], these models are limited to the melt only. Since a TMCZ growth furnace is a highly non-linear and conjugated system, 3D global modeling is obviously necessary. Liu and Kakimoto [7] recently proposed a 3D global model that makes 3D global modeling be feasible with moderate requirements of computer resources and computation time. For the purpose of a better understanding of realistic phenomena and the physics of a TMCZ growth process, we applied this 3D global model to analyzing a small TMCZ furnace in this paper.

* Corresponding author. Tel.: +81 92 583 7741; fax: +81 92 583 7743.
E-mail address: kakimoto@riam.kyushu-u.ac.jp (K. Kakimoto).

0017-9310/$ - see front matter © 2005 Elsevier Ltd. All rights reserved.
doi:10.1016/j.ijheatmasstransfer.2005.04.030

Nomenclature

$\vec{B}$	magnetic flux density (T)
c	heat capacity (J/kg K)
$\vec{E}$	electric field (m kg/s^3 A)
$\vec{g}$	gravitational acceleration (m/s^2)
$\vec{J}$	electrical current density (kg/s^3 A Ω)
k	thermal conductivity (W/m K)
$\vec{n}$	unit normal vector
p	melt pressure (P_a)
r	radial coordinate (m)
R_{cry}	crystal radius (m)
T	temperature (K)
T_m	melting temperature of silicon (K)
U_M	velocity of melt relative to the magnetic field (m/s)
$\vec{V}$	melt velocity (m/s)

Greek symbols

β_T	thermal expansion coefficient (1/K)
Φ	electrical potential (m^2 kg/s^3 A)
μ	melt viscosity (kg/m s)
ρ	melt density (kg/m^3)
σ_m, σ_s	electrical conductivities of molten silicon and crystal (S/m)

Subscripts

m	melt
s	solid
n	normal direction

2. Governing equations of melt flow under a transverse magnetic field

The imposed magnetic field influences the growth process through the melt convection in the crucible by exerting Lorentz force on the molten silicon. With the assumptions of a quasi-steady system and incompressible laminar flow of the melt, the governing equations for the melt convection under the influence of a transverse magnetic field are as follows:

$$\nabla \cdot \vec{V} = 0, \tag{1}$$

$$\rho \vec{V} \cdot \nabla \vec{V} = -\nabla p + \nabla \cdot [\mu(\nabla \vec{V} + \nabla \vec{V}^{\mathrm{T}})] - \rho \vec{g} \beta_T (T - T_m) + \vec{J} \times \vec{B}, \tag{2}$$

$$\rho c \vec{V} \cdot \nabla T = \nabla \cdot (k \nabla T). \tag{3}$$

The last two terms in Eq. (2) are the thermal buoyancy and the Lorentz force.

In order to determine the Lorentz force exerted on the molten silicon, we need to solve the electrical field induced by the imposed magnetic field and governed by

$$\nabla \cdot \vec{J} = 0, \tag{4}$$

$$\vec{J} = \sigma_m(\vec{E} + \vec{U}_M \times \vec{B}) \quad \text{in the melt,} \tag{5.1}$$

$$\vec{J} = \sigma_s(\vec{E} + \vec{U}_M \times \vec{B}) \quad \text{in the crystal,} \tag{5.2}$$

$$\vec{E} = -\nabla \Phi. \tag{6}$$

The effect of the induced magnetic field on the applied field is neglected. The crucible, pulling rod and ambient gas are electrically insulated, while the silicon crystal is an electrical conductor. Therefore, the calculation of electromagnetic field is limited to the melt–crystal domain.

The boundary conditions are given as follows for the electromagnetic field. On all of the external boundaries of the melt–crystal domain, a non-penetration condition for electrical current density is imposed, i.e.,

$$\vec{J} \cdot \vec{n} = 0, \tag{7.1}$$

or in the form

$$\frac{\partial \Phi}{\partial n} = (\vec{U}_M \times \vec{B}) \cdot \vec{n}. \tag{7.2}$$

On the melt–crystal interface,

$$(\vec{J} \cdot \vec{n})_s = (\vec{J} \cdot \vec{n})_m, \tag{8.1}$$

or in the form

$$\sigma_s \left[(\vec{U}_M \times \vec{B})_n - \frac{\partial \Phi}{\partial n} \right]_s = \sigma_m \left[(\vec{U}_M \times \vec{B})_n - \frac{\partial \Phi}{\partial n} \right]_m. \tag{8.2}$$

3. Results and discussion

In this section, results of analysis of a silicon TMCZ furnace obtained by using the proposed 3D global model [7] are presented. The magnetic field is homogeneous with intensity of 0.1 T oriented in the x-direction. The crystal diameter is 32 mm. The diameter of the crucible inside wall is 64 mm. The depth of the melt is 28 mm. A typical crystal growth rate of 0.3 mm/min is applied. The crucible and the crystal are non-rotating. The material properties of the constituents of the furnace are listed in Table 1.

The 3D domain includes the crystal, melt, crucible and heater. The discrete system is constituted by 364,500 control volumes and 22,400 radiative surface elements in the 3D domain and by 6170 control volumes and 1609 radiative surface elements in the 2D domain. A computation run takes about 10 days on a HP ITANIUM-2 workstation with memory capacity of 2.6 gigabytes.

Table 1
Material properties and process parameters

Density
$\rho = 2520$ kg/m^3 (melt), $\rho = 2305$ kg/m^3 (crystal),
$\rho = 2190$ kg/m^3 (quartz crucible),
$\rho = 2262$ kg/m^3 (heater, pedestal, seed/puller, heat insulators)

Thermal conductivity
$k = 54$ W/m K (melt), $k = 25.7$ W/m K (crystal),
$k = 5.0$ W/m K (quartz crucible),
$k = 42$ W/m K (heater, pedestal, seed/puller, heat insulators)

Heat capacity
$c = 1000$ J/kg K (melt), $c = 946$ J/kg K (crystal),
$c = 1525$ J/kg K (quartz crucible),
$c = 2050$ J/kg K (heater, pedestal, seed/puller, heat insulators)

Emissivity factor
$\varepsilon = 0.30$ (melt), $\varepsilon = 0.58$ (crystal), $\varepsilon = 0.35$ (chamber walls),
$\varepsilon = 0.50$ (quartz crucible),
$\varepsilon = 0.80$ (heater, pedestal, seed/puller, heat insulators)

Electrical conductivity
$\sigma_m = 1.29 \times 10^6$ S/m (melt), $\sigma_s = 1.20 \times 10^5$ S/m (crystal)

Melting temperature of silicon $T_m = 1685$ K
Thermal expansion coefficient of melt $\beta_T = 1.4 \times 10^{-4}$ K^{-1}
Latent heat of solidification $\Delta H = 1411 \times 10^3$ J/kg
Dynamic viscosity of melt $\mu = 7.0 \times 10^{-4}$ kg/m s
Coolant temperature $T_W = 350$ K
Stefan–Boltzmann constant $\sigma = 5.6696 \times 10^{-8}$ W m^{-2} K^{-4}

Fig. 1 shows the electrical scalar potential distribution in the melt–crystal domain. The field is symmetric about the plane $x = 0$, and the gradient in the crystal domain is quite small compared to that in the melt domain. The overall temperature distributions in symmetric planes $x = 0$ and $y = 0$ are respectively shown in the right and left half-planes of Fig. 2, while a local temperature distribution in the 3D domain is presented in Fig. 3. The thermal field is symmetric about both plane $x = 0$ and plane $y = 0$. Only the thermal fields on the half-planes are therefore shown in Fig. 2 for both symmetric planes $x = 0$ and $y = 0$. From Fig. 3, it is apparent that the thermal field in the core regions is characterized by three-dimensionality, especially in the

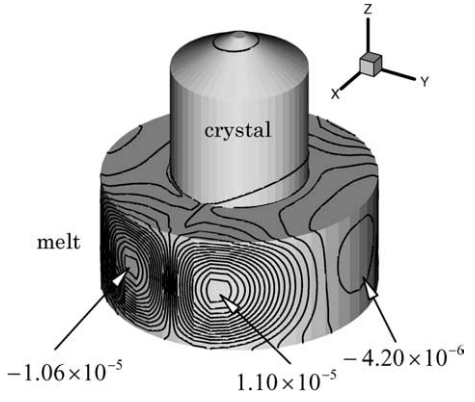

Fig. 1. Contour lines of electrical scalar potential plotted every 8×10^{-7} m^2 kg/s^3 A.

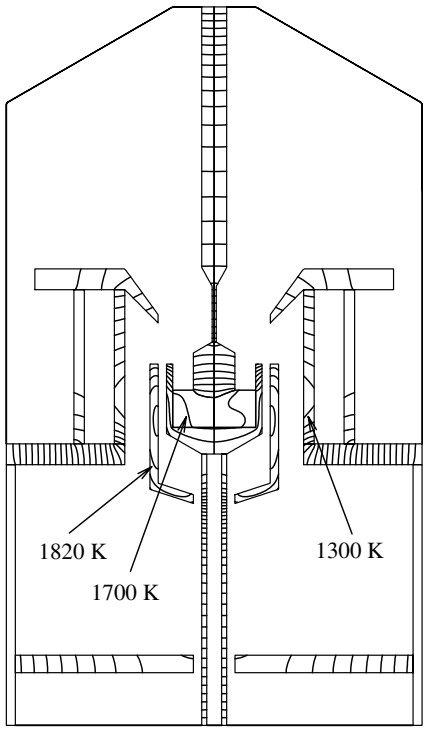

Fig. 2. Isotherms in symmetric planes $x = 0$ (right half-plane) and $y = 0$ (left half-plane) plotted every 40 K.

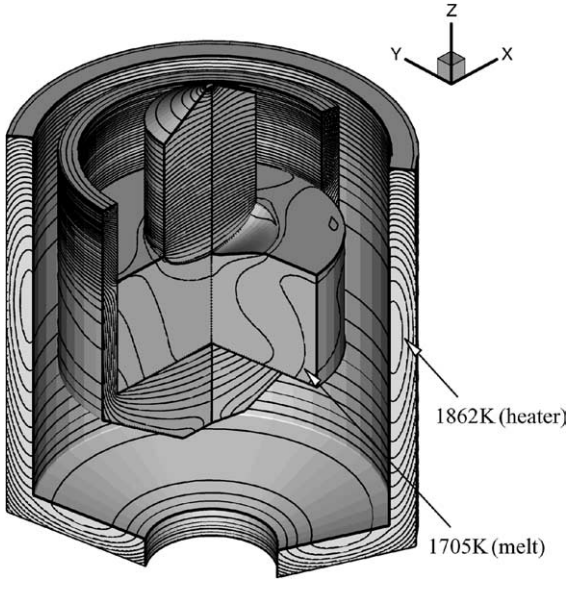

Fig. 3. Local temperature distribution in the crystal, melt, crucible and heater. Isotherms are plotted every 7.5 K.

melt. Even the inhomogeneity of temperature distribution in the azimuthal direction on the outside wall of crucible is noticeable. The highest temperature occurring on the inside wall of the heater is as high as 1862 K. The converged value of the heater input power obtained from the modeling is 16.0 kW for this test case.

Fig. 4 shows the melt flow, thermal field and melt–crystal interface profiles in the half-planes of $x = 0$ and $y = 0$. The melt–crystal interface corresponds to the isotherm of 1685 K. A pair of strong vortexes occupies the symmetric plane $x = 0$, while in the symmetric plane $y = 0$, the melt flows downward to the bottom of the crucible. This is due to the influence of the transverse magnetic field that leads the melt flows toward the symmetric plane $y = 0$ on the melt surface and flows away from it at the bottom. Meanwhile, the velocity component in the x-direction nearly vanishes. The convective flow structure of melt can be seen in Fig. 5(a), which shows the convective flow patterns of melt in three representative planes that are respectively located at 5%, 50% and 95% depth of melt in the crucible. Corresponding to the three-dimensional convective flow pattern of melt, the patterns of the temperature distribution in the half-planes $x = 0$ and $y = 0$, as shown in Fig. 4, and the temperature distributions in the three horizontal planes at different depths in the melt, as shown in Fig. 5(b), are distinctly different.

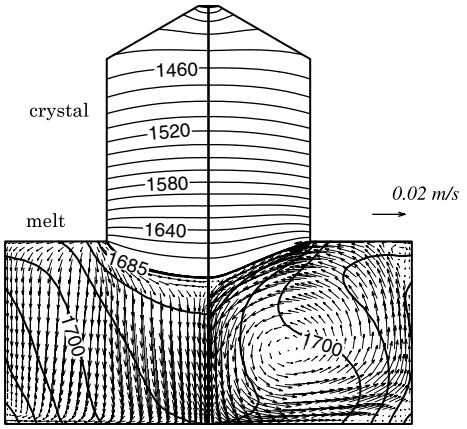

Fig. 4. Melt flow, thermal field and melt–crystal interface profiles in symmetric planes $x = 0$ (right half-plane) and $y = 0$ (left half-plane). Isotherms are plotted every 15 K in the crystal and every 5 K in the melt.

As a result of the three-dimensional feature of the convective flow and thermal field in the melt, the melt–crystal interface is also characterized by distinct three-dimensionality. This feature can be seen in Fig. 6. Fig. 6(a) shows the three-dimensional shape of the melt–crystal interface and the temperature distribution on the melt surface as well as on the interface. Fig. 6(b) shows the distributions of interface deflection in the azimuthal direction at three radial locations where

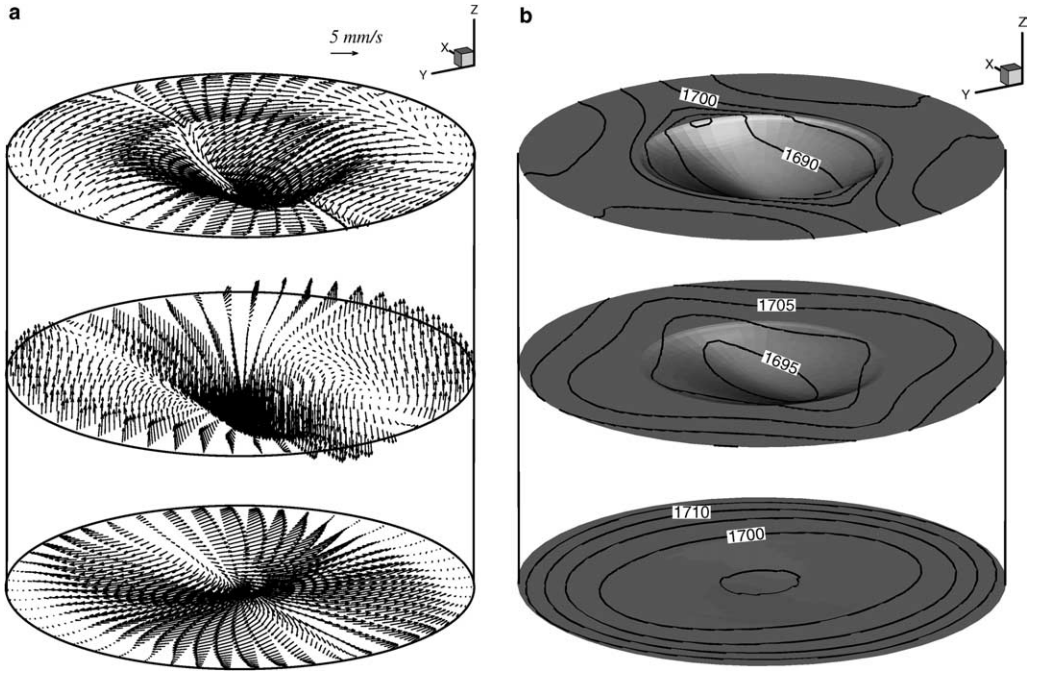

Fig. 5. Convective flow patterns and temperature distributions in three planes at 5%, 50% and 95% depth of melt (from top to bottom). (a) Convective melt flow. (b) Temperature distribution. Isotherms are plotted every 5 K.

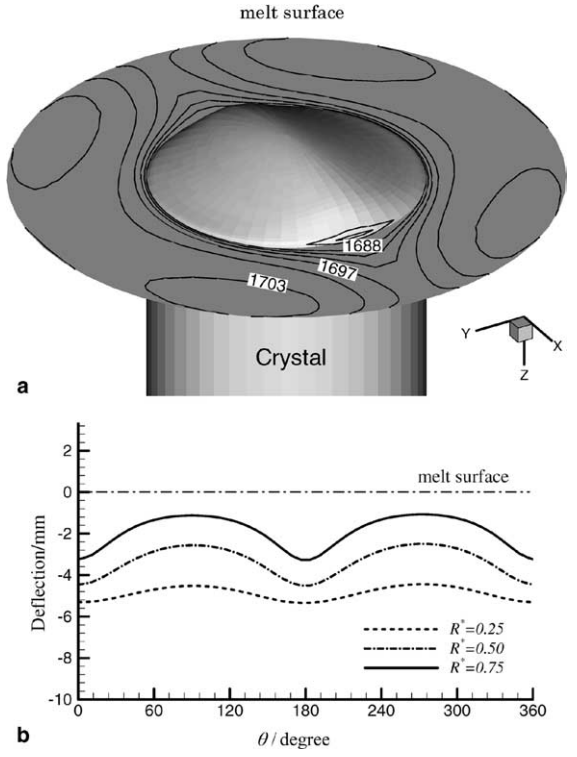

Fig. 6. The melt–crystal interface shape. (a) A 3D view of the melt–crystal interface and the temperature distribution on the melt top surface as well as on the interface. Isotherms are plotted every 3 K. (b) Interface deflection distributions in the azimuthal direction at three radial locations.

$R^* = 0.25$, 0.50, 0.75, respectively, and $R^* = r/R_{cry}$. An elliptic region of low temperature is generated on the melt surface in the magnetic field direction, as shown in Fig. 6(a), resulting in the ridge of the interface in the x-direction. The calculated melt–crystal interface is an isothermal surface except in the narrow region near the crystal edge where the temperature is not precisely equal to the melting point of silicon because of the assumption of axisymmetric geometry of the model. However, as can be known from Fig. 6(a) by noting the temperature field around the crystal, the calculated interface shape is very close to the surface shape obtained by identification to the isothermal surface of melting temperature (1685 K), which is slightly elliptic. We can thus take the calculated interface shape by using this model as a good approximation of the actual one. A clearer image about the three-dimensional character of the interface can be obtained in Fig. 6(b), in which it is shown that the difference in interface deflection over the circumference can be as large as one eighth of the crystal radius and more than one third of the maximal deflection at the axis.

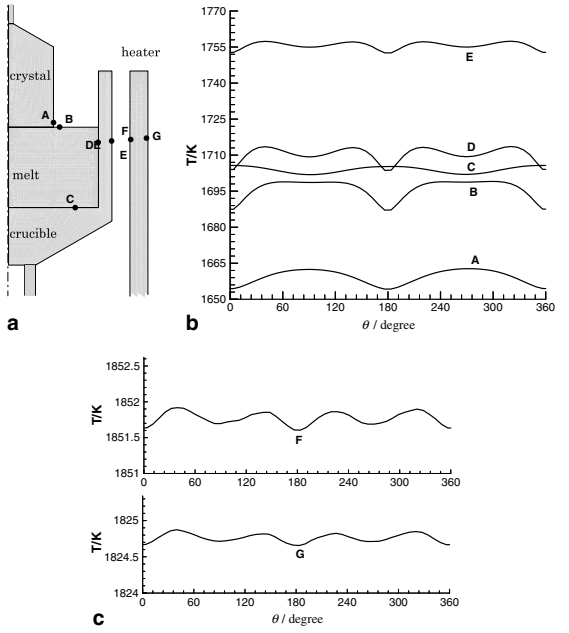

Fig. 7. Non-uniform temperature distributions in the azimuthal direction. (a) Locations under consideration. (b) A, the crystal sidewall; B, the melt top surface; C, the melt bottom; D, the melt sidewall; E, the crucible outside wall. (c) F, the inside wall of the heater; G, the outside wall of the heater.

In order to examine the non-uniformity of the thermal field in the azimuthal direction, we select seven typical monitoring locations for study. The monitoring locations are on the crystal sidewall, the melt surface, the melt bottom, the melt sidewall, the crucible outside wall and the inside and outside walls of the heater, as illustrated in Fig. 7(a). The non-uniform temperature distributions in the azimuthal direction at these locations are shown in Fig. 7(b) and (c). From Fig. 7(b), we can notice distinct non-uniformity of the temperature distribution in the azimuthal direction. The maximal difference in temperature over the circumference occurs on the melt surface with a value as high as 13.2 K. We can also confirm the complexity of the temperature distribution in the melt by observing the different curve shapes of the temperature distribution in the azimuthal direction at different locations in the melt, as shown in Fig. 7(b) by curves B, C and D. This diversity is due to the convective flow of the melt under the influence of the transverse magnetic field. The non-uniformity is small at the melt bottom (curve C) compared to that at the melt top surface (curve B) and that at the melt sidewall (curve D), and this non-uniformity decreases further with increase in distance from the melt domain. This can be confirmed from Fig. 7(b), in which it can be seen that the non-uniformity of 10.0 K at the melt side-

wall (location D) decreases to 4.9 K at the outside wall of the crucible (location E). Furthermore, this non-uniformity becomes obscure in the heater. As can be seen in Fig. 7(c), the maximal temperature difference over the circumference is about 0.3 K on the inside wall and deceases to about 0.2 K on the outside wall of the heater. This is partly because the furnace is very small. The non-uniformity might be more distinct in a furnace with larger dimensions. However, we can reasonably expect that the non-uniformity in the heat insulators, which are far away from the melt domain, should be more obscure if fully 3D global modeling is performed under this growth condition. This confirms that the proposed 3D global model is reasonable and efficient.

4. Conclusions

A 3D global analysis was conducted using the proposed model for a silicon CZ growth furnace in a transverse magnetic field. The modeling was conducted with moderate requirements of computer resources and computation time. The global iteration is proved to be satisfactorily stable. Three-dimensional features of the melt flow in the crucible and the thermal field in the furnace, along with the 3D melt–crystal interface shape, were reasonably reproduced in the modeling. The results of simulation also revealed that 3D features are mainly displayed in the core region of a CZ furnace and gradually disappear with increase in distance from the melt domain. The influence of the transverse magnetic field was analyzed.

Acknowledgement

This work was supported by a Grant-in Aid for Scientific Research (B) 14350010 from the Japanese Ministry of Education, Science, Sports and Culture.

References

[1] K. Kakimoto, Oxygen distribution in silicon melt under inhomogeneous transverse magnetic fields, J. Cryst. Growth 230 (2001) 100–107.
[2] K. Kakimoto, A. Tashiro, T. Shinozaki, H. Ishii, Y. Hashimoto, Mechanisms of heat and oxygen transfer in silicon melt in an electromagnetic Czochralski system, J. Cryst. Growth 243 (2002) 55–65.
[3] K. Kakimoto, Effects of rotating magnetic fields on temperature and oxygen distributions in silicon melt, J. Cryst. Growth 237–239 (2002) 1785–1790.
[4] H. Ozoe, M. Iwamoto, Combined effects of crucible rotation and horizontal magnetic field on dopant concentration in a Czochralski melt, J. Cryst. Growth 142 (1994) 236–244.
[5] A. Krauze, A. Muiznieks, A. Muhlbauer, Th. Wetzel, W.v. Ammon, Numerical 3D modeling of turbulent melt flow in a large CZ system with horizontal DC magnetic field, I: flow structure analysis, J. Cryst. Growth 262 (2004) 157–167.
[6] A. Krauze, A. Muiznieks, A. Muhlbauer, Th. Wetzel, E. Tomzig, L. Gorbunov, A. Pedchenko, J. Virbulis, Numerical 3D modeling of turbulent melt flow in a large CZ system with horizontal DC magnetic field, II: comparison with measurements, J. Cryst. Growth 265 (2004) 14–27.
[7] L.J. Liu, K. Kakimoto, Partly three-dimensional global modeling of a silicon Czochralski furnace I. Principles, Formulation and Implementation of the Model, Int. J. Heat Mass Transfer, in press, doi:10.1016/j.ijheatmasstransfer.2005.04.031.